

UC San Diego

UC San Diego Previously Published Works

Title

Microstructural analysis of skeletal muscle force generation during aging

Permalink

<https://escholarship.org/uc/item/7tc2k776>

Journal

International Journal for Numerical Methods in Biomedical Engineering, 36(1)

ISSN

2040-7939

Authors

Zhang, Yantao
Chen, Jiun-Shyan
He, Qizhi
[et al.](#)

Publication Date

2020

DOI

10.1002/cnm.3295

Peer reviewed

Microstructural Analysis of Skeletal Muscle Force Generation During Ageing

Yantao Zhang^a, Jiun-Shyan Chen^{a,*}, Qizhi He^a, Xiaolong He^a, Ramya Rao Basava^a, John Hodgson^b, Usha Sinha^c, Shantanu Sinha^d

^a Department of Structural Engineering, University of California San Diego, San Diego, CA, USA

^b Department of Integrative Biology and Physiology, University of California Los Angeles, Los Angeles, CA, USA

^c Department of Physics, San Diego State University, CA, USA

^d Department of Radiology, University of California San Diego, San Diego, CA, USA

Zhang, Y., Chen, J. S., He, Q., He, X., Basava, R. R., Hodgson, J., Sinha, U., Sinha, S., “Microstructural Analysis of Skeletal Muscle Force Generation During Ageing,” International Journal for Numerical Methods in Biomedical Engineering, DOI: 10.1002/cnm.3295, 2019.

Abstract

Human ageing results in a progressive decline in the active force generation capability of skeletal muscle. While many factors related to the changes of morphological and structural properties in muscle fibers and the extracellular matrix (ECM) have been considered as possible reasons for causing age-related force reduction, it is still not fully understood why the decrease of force generation under eccentric contraction (lengthening) is much less than that under concentric contraction (shortening). Biomechanically, it was observed that connective tissues (endomysium) stiffen as ages, and the volume ratio of connective tissues exhibit an age-related increase. However, limited skeletal muscle models take into account the microstructural characteristics as well as the volume fraction of tissue material. This study aims to provide a numerical investigation in which the muscle fibers and the ECM are explicitly represented to allow quantitative assessment of the age-related force reduction mechanism. To this end, a honeycomb-like, fiber-level microstructure is constructed and modeled by a pixel-based Reproducing Kernel Particle Method (RKPM), which also allows modeling of smooth transition in biomaterial properties across material interfaces. The numerical investigation reveals that the increased stiffness of the passive materials of muscle tissue reduces the force generation capability under concentric contraction while maintains the force generation capability under eccentric contraction. The proposed RKPM microscopic model provides effective means for the cellular-scale numerical investigation of skeletal muscle physiology.

Key Words: Ageing; Skeletal muscle; Force generation; Connective tissue; Microstructure; Numerical simulation; Reproducing Kernel Particle Method

1. Introduction

The performance and functioning of skeletal muscle deteriorate with age, causing a significantly negative impact on people's daily life. It is therefore important to understand the roles of different musculoskeletal factors (such as material properties, microstructures, and morphologies of muscle tissues) in affecting the force generation capacity. It is widely accepted that the force generation capability of skeletal muscle decreases with ageing. The reasons behind the age-associated force reduction could be the loss of mass in contractile components, loss of motor units (neural-excitation), alterations in fiber types and passive material properties, changes in the specific fiber tension and contractile velocity, and fatty inclusions, etc. [1–3]. It was also observed that the reduction of force exhibits significant differences between eccentric and concentric contraction [4–7], where the loss of force generation under concentric contraction is usually greater than that under eccentric contraction, and sometimes even no age-related difference in force production during eccentric contraction is observed [8,9]. Nevertheless, limited quantitative studies have been conducted on the causal relationship between the previously mentioned determinants of age-related force loss and the fact that muscle tends to maintain force generation with ageing under eccentric contraction.

Skeletal muscle consists of muscle fibers and an extracellular matrix (ECM), and thus, the overall mechanical properties of skeletal muscle tissue are determined by the individual properties of these two components and the interactions between them [10]. At the cellular level, the muscle tissue is a honeycomb-like composite material with the connective tissue (CT) phase, i.e. endomysium, and the muscle fiber phase [11–13]. In particular, CT is postulated to play an important role in myofascial force transmission of muscle, providing essential structural support to ensure muscle's integrity, and protecting muscle cells from damages during muscle contraction [13,14]. In terms of ageing effects, two important biological observations about CT have been reported: (1) the stiffness of CT in skeletal muscle increases with ageing [15–18], and (2) the volume ratio or thickness of connective tissue (endomysium) increases with ageing [15,17]. Thus, in this study, we investigate how these age-related microstructural variations could affect the biomechanical behaviors of skeletal muscle, especially the force generation capacity.

During the last few decades, computational modeling of skeletal muscles has advanced significantly, from the most simplified 1D lumped-parameter model [19] to the 3D sophisticated

muscle models represented by a fiber-reinforced composite materials based on fiber-level constitutive models [20–25]. These macro-scale models enable a systematic study of the structural and functional properties of skeletal muscles. However, the simulation-based investigation into the effects of microstructural variations, such as microstructural composition and material properties on the skeletal muscle functionality, is less complete. A micromechanical model based on the concept of repeating unit cells extracted from histological cross-sections of rabbit muscles [26] was proposed to study the effects of microstructural geometry in both fiber and fascicle levels on the macroscopic along-fiber shear modulus of skeletal muscle. Virgilio et al. [27] utilized an agent-based model to generate honeycomb-like micromechanical models of skeletal muscle and studied the influences of disease-associated alterations in muscle microstructure on muscle’s macroscopic along-fiber shear modulus. Recently, Spyrou et al. proposed analytical and numerical homogenization models based on the honeycomb-like microstructure to bridge various length scales of skeletal muscle [28,29].

In this study, we proposed a micromechanical computational model based on the honeycomb-like structure for skeletal muscle to examine the effects of age-related changes in the material properties (muscle fiber and CT) and volume fraction on the force generation capability of skeletal muscle, with a focus on understanding the mechanism causing the force reduction difference between concentric and eccentric contraction. Further, the proposed numerical model is constructed using the Reproducing Kernel Particle Method (RKPM) [30–32], which effectively models smooth transition of biomaterial properties across material interfaces and allows model discretization to be obtained directly using the pixel points from CT scans and avoids the complexity of constructing mesh-based models [33,34].

The rest of this paper is organized as the followings. In Section 2, the construction of pixel-based meshfree models, material models and the loading conditions used in the simulations are introduced. Numerical validation of the meshfree computational framework is first presented in Section 3, followed by the discussion of numerical results of the force generation of contracted skeletal muscle microstructure in the same section. The conclusions are given in Section 4.

2. Methods

2.1. Model Construction from Images

In this work, a honeycomb-like microstructure of skeletal muscle tissue is constructed based on a representative image of the cellular-scale cross section of skeletal muscle tissue. A region based level-set algorithm [35] is employed for image segmentation. In the honeycomb-like microstructure, two material phases are considered, i.e. the CT (endomysium) phase and the muscle fiber phase. The two-dimensional (2D) segmented microstructure is then extruded along the out-of-plane direction (the z -direction) to generate the three-dimensional (3D) model. Here, the pixel points used for image segmentation are then readily used as meshfree nodes for the discretization in the RKPM simulation model. The model construction processes are summarized in Figure 1 as follows. Figure 1a is extracted from [12], which shows a representative unit cell of muscle fibers separated by the connective tissue, i.e. the endomysium. Figure 1b shows the level-set segmented images and the associated pixel points. The 3D model is generated by extruding the 2D model as shown in Figure 1c, and the dimension of the honeycomb model is normalized to $1 \times 1 \times 1$.

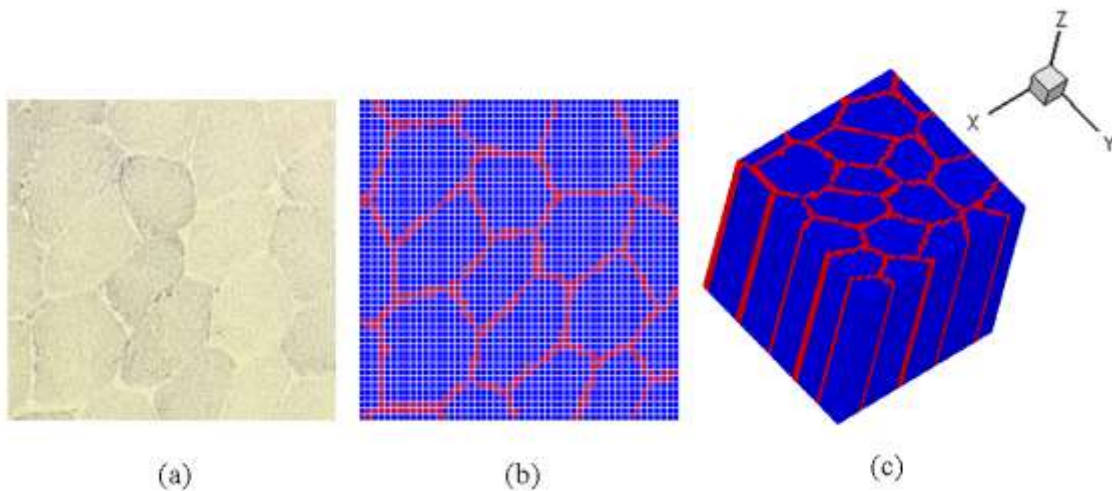


Figure 1 The procedure of constructing the 3D model from the 2D images of the cellular-scale cross section of skeletal muscle tissue [12]. (a) the cross-sectional image of a representative unit cell of the muscle tissue, (b) level-set segmented cross section, and (c) 3D model produced by extruding the 2D model along the z -direction. Blue points denote the muscle fiber phase and red points denote the connective tissue phase.

In this work, an RKPM based approximation and discretization [30,31], see Appendix A, together with the stabilized conforming nodal integration (SCNI) [32] are employed to solve for the hyperelasticity boundary value problem. Note that biological material is commonly modeled as nearly incompressible hyperelasticity [36], which usually requires special treatment to handle the incompressibility in structural analysis [37]. It has been shown that RKPM with SCNI provides proper numerical treatment of incompressibility, see details in [31,32,38,39]. Moreover, the arbitrarily high-order continuity of RKPM approximation allows smooth transition of biomaterial properties across material interfaces to be effectively modeled.

2.2. Material Models

In skeletal muscle, the contractile muscle fibers can generate positive stress even in the undeformed state, whereas CT is treated as passive material which deforms in response to the applied loads. Here, the CT material is modeled by a cubic polynomial hyperelastic model with the uniaxial tension-compressive behavior shown in Figure 2a where λ is the stretch ratio. Following [19,21,40], the active stress-stretch curve of the skeletal muscle fiber and the combined active and passive response are shown in Figure 2b. The operation region of skeletal muscle [41], defined as $[0.9, 1.5]$ in this work, is shaded in Figure 2b, where $\lambda < 1.0$ and $\lambda > 1.0$ represents concentric and eccentric contractions, respectively.

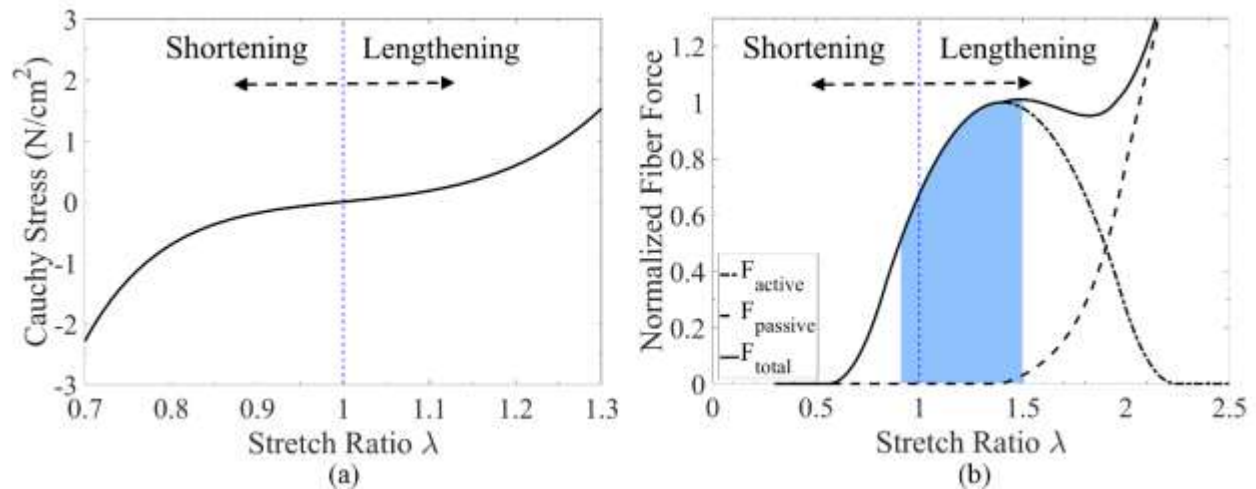


Figure 2 (a) The uniaxial stress-stretch relation of a cubic polynomial hyperelastic material model for connective tissue, and (b) the normalized active and passive mechanical response of the muscle fiber model [19,21,40].

The strain energy density function of the muscle fiber hyperelastic model is decomposed into the isotropic and the anisotropic parts,

$$W_{\text{fiber}} = W_{\text{iso}}(\bar{I}_1, \bar{I}_2, J) + W_{\text{ani}}(\lambda), \quad (1)$$

where λ is the along-fiber stretch ratio, \bar{I}_1, \bar{I}_2 are the reduced invariants of right Cauchy-Green strain tensor $\mathbf{C}^T = \mathbf{F}^T \mathbf{F}$, defined as $\bar{I}_1 = J^{-2/3} I_1$ and $\bar{I}_2 = J^{-4/3} I_2$ with $I_1 = \text{tr}(\mathbf{C})$ and $I_2 = 0.5[I_1^2 - \text{tr}(\mathbf{C}^2)]$, and $J = \det(\mathbf{F})$ is the relative change in volume. Here \mathbf{F} is the deformation gradient defined as $\mathbf{F} = \frac{\partial \mathbf{x}}{\partial \mathbf{X}}$, where \mathbf{x} and \mathbf{X} are the material position vectors in the current and initial configuration, respectively. The isotropic part, associated with the contribution of membrane structures and biofluids contained in a muscle fiber [28], is given by a quadratic polynomial type function,

$$W_{\text{iso}} = \sum_{i+j=1}^2 C_{ij} (\bar{I}_1 - 3)^i (\bar{I}_2 - 3)^j + \frac{K}{2} (J - 1)^2, \quad (2)$$

where the material constants C_{ij} and the bulk modulus K are associated with the resistance against the deviatoric and volumetric deformations, respectively. The anisotropic strain energy density function W_{ani} is introduced to describe the behavior of the fiber's contractile behavior [40],

$$\lambda \frac{\partial W_{\text{ani}}}{\partial \lambda} = \sigma_{\text{max}} \frac{\lambda}{\lambda_0} (\alpha f_{\text{active}} + f_{\text{passive}}), \quad (3)$$

where σ_{max} is the fiber maximum isometric stress, $\lambda_0 = 1.4$ is chosen as the optimal stretch ratio at which muscle fiber generates maximum force [21,40], as shown in Figure 2b, and α is the activation level ranging in $[0, 1]$. For instance, $\alpha = 0$ indicates the muscle fiber is in a completely passive state, and $\alpha = 1$ indicates a fully activated state. f_{active} and f_{passive} are the normalized active and passive parts of the muscle fiber force [21,40], respectively, expressed as

$$f_{active} = \begin{cases} 9(\lambda^* - 0.4)^2 & \lambda^* \leq 0.6 \\ 1 - 4(1 - \lambda^*)^2 & 0.6 < \lambda^* \leq 1.4 \\ 9(\lambda^* - 1.6)^2 & \lambda^* > 1.4 \end{cases} \quad (4)$$

$$f_{passive} = \begin{cases} 0 & \lambda^* \leq 1 \\ \gamma_1 (e^{\gamma_2(\lambda^*-1)} - 1) & 1 < \lambda^* \leq 1.4 \\ (\gamma_1 \gamma_2 e^{0.4\gamma_2}) \lambda^* + \gamma_1 ((1 - 1.4\gamma_2) e^{0.4\gamma_2} - 1) & \lambda^* > 1.4 \end{cases} \quad (5)$$

where λ^* is the normalized stretch as $\lambda^* = \lambda/\lambda_0$. The diagram of f_{active} and $f_{passive}$ are plotted in Figure 2b. It is noted that the passive part $f_{passive}$ is mainly contributed by the protein inside the sarcomeres called titin [42–44], and the adopted values of coefficients γ_1 and γ_2 associated with different age groups are discussed in the following section.

For the CT phase, a cubic polynomial hyperelastic material model is adopted [45,46],

$$W_{CT} = \sum_{i=1}^3 C_{i0} (\bar{I}_1 - 3)^i + \frac{K}{2} (J - 1)^2 \quad (6)$$

The bulk modulus K used in Eqs. (2) and (6) are much bigger than the parameters C_{ij} so that the material is nearly incompressible. The nonlinear response introduced by the higher order terms in the polynomial of the first reduced invariant is able to represent softer low-strain region and stiffer high-strain region [19].

2.3. Material Parameters

Titin, the muscle protein inside the sarcomeres, plays an important role in the passive stiffness of the muscle fiber [42–44]. It was reported that the titin-based passive stiffness of adult muscle is more than 50% greater than that of the young muscle [47]. To represent the age-related increase in titin's stiffness at the cellular level, the titin related parameter (γ_1 in Eq. (5)) associated with the passive fiber stiffness of Adult and Old muscle fibers is respectively set as one-and-a-half and two times of that of the Young muscle, as listed in Table 1 [21,40].

As muscle fiber has little resistance under compression in the fiber direction, experimental data from skeletal muscle tissue under uniaxial compression along the fiber direction can be used to calibrate the material parameters of the CT material models [28,48,49]. Figure 3a summarizes

the experimental data extracted from literatures for the uniaxial compressive experiments in the muscle fiber direction, conducted on rat tibialis anterior muscle [50,51], porcine, bovine, and ovine muscles [52,53], and human forearm muscle [54]. The experimental data shows a large variation in stress-stretch relations. Previous studies reported that the stiffness of CT (endomysium) of old muscle is about twofold of that of the adult's [15–17]. Wood et al. found that the stiffness of ECM of old muscle increases by twelvefold, compared to that of the adult's [18]. Given the large variation in stress-stretch relations [50–54] and the observations on stiffness relations between muscles of different age groups [15–18], three sets of CT materials with different material properties are defined corresponding to Young, Adult, and Old muscles in Table 2, where the CT stiffness of the Adult and Old muscles is set as four and eight times of that of the Young one, respectively. They are denoted as “Soft CT”, “Medium Stiff CT”, and “Stiff CT”, respectively, and their corresponding stress-stretch relations fitted using the CT model in Eq. (6) are shown in Figure 3a. It is obvious that muscle units with stiffer materials yield larger stress at any given stretch ratio in both tensile and compressive deformations.

The isotropic material property of the Young muscle fiber is defined as twice of that of the Young CT [28] and the isotropic material property of Adult and Old muscle fibers is set as two and three times of that of the Young muscle fiber, respectively, as given in Table 3. Figure 3b shows the stress-stretch curves associated with the isotropic part of the adopted muscle fiber model in Eq. (2) for Young, Adult and Old muscles, denoted by “Soft”, “Medium Stiff”, and “Stiff” according to their stiffness, respectively. The corresponding material parameters of the cubic hyperelastic model for CT (Eq. (6)) and the quadratic hyperelastic model for the isotropic part of muscle fibers (Eq. (2)) are listed in Table 2 and Table 3, respectively.

As discussed above, the passive stiffness (PS) of the whole muscle tissue is contributed by passive components of fiber and CT. Overall, three sets of PS are defined corresponding to Young, Adult, and Old muscles for the following numerical studies. They are denoted as “Low PS”, “Medium PS”, and “High PS”, respectively, as listed in Table 4. For instance, “Low PS” indicates a combination of Soft titin-based passive fiber stiffness, Soft CT stiffness, and Soft fiber's isotropic stiffness.

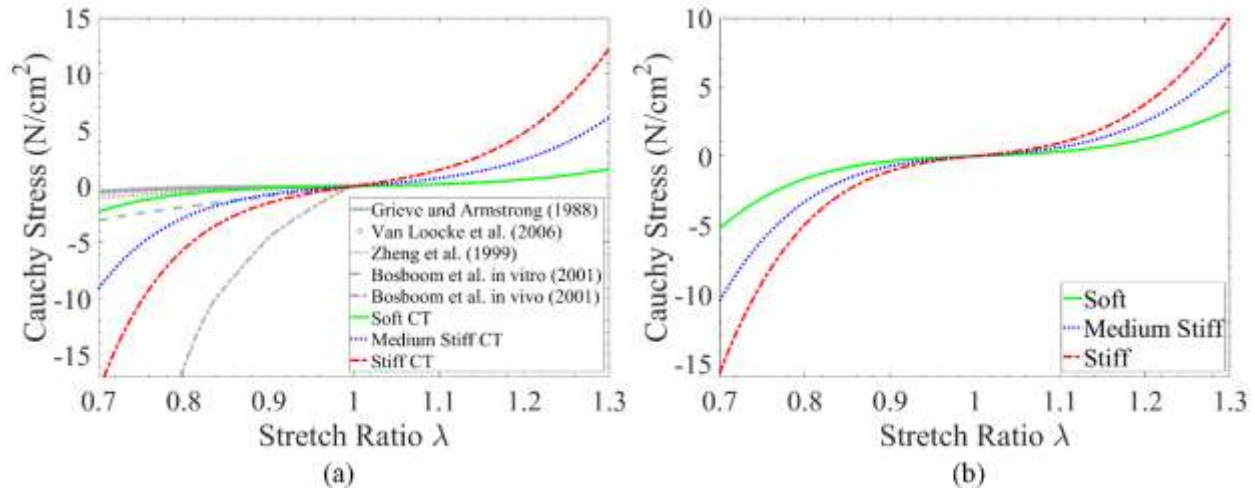


Figure 3 Stress-stretch relation of muscle materials under uniaxial deformation: (a) the comparison of compressive stress-stretch experimental data of muscle tissue and the response of the connective tissue (CT) material model fitted using Eq. (6) with different stiffness; (b) the stress-stretch response of the isotropic part of the muscle fiber model in Eq. (2) with different stiffness; The stretch ratio is along the direction in which the material is stretched or compressed.

Table 1 - Material parameters of the normalized passive fiber force in Eq. (5) with different titin stiffness [21,40]

Age	Titin Stiffness	γ_1	γ_2
Young	Soft	0.05	6.6
Adult	Medium Stiff	0.075	6.6
Old	Stiff	0.1	6.6

Table 2 - Material parameters of the connective tissue (CT) model in Eq. (6) with different stiffness (unit: N/cm²)

Age	CT Stiffness	C_{10}	C_{20}	C_{30}	K
Young	Soft	0.36	1.63	0.95	5×10^3
Adult	Medium Stiff	1.42	6.50	3.80	2×10^4
Old	Stiff	2.84	13.00	7.60	4×10^4

Table 3 - Material parameters of the isotropic part of the muscle fiber model in Eq. (2) with different stiffness (unit: N/cm²)

Age	Fiber's Isotropic Stiffness	C_{10}	C_{01}	C_{20}	C_{11}	C_{02}	K
Young	Soft	0.14	0.40	0.005	5.05	0.003	10^4
Adult	Medium Stiff	0.28	0.80	0.010	10.10	0.006	2×10^4
Old	Stiff	0.42	1.20	0.015	15.15	0.009	3×10^4

Table 4 - Summary of the employed passive stiffness of the muscle tissue components for Young, Adult, and Old muscles

Age	Passive Stiffness	Titin Stiffness	CT Stiffness	Fiber's Isotropic Stiffness
Young	Low	Soft	Soft	Soft
Adult	Medium	Medium Stiff	Medium Stiff	Medium Stiff
Old	High	Stiff	Stiff	Stiff

2.4. Loading Condition for Force Generation Analysis

For simulation convenience, we adopt two loading stages although these two loading mechanisms co-exist in reality. In the first loading stage, the model is constrained at both ends (i.e., the planes of $z = 0$ and $z = 1$ in Figure 4) and the muscle activation level is taken as 1, representing fully activated muscle fibers without deformation. In the second stage, a uniaxial compression (concentric contraction) or tension (eccentric contraction) is applied to the model so that the model shortens or lengthens to certain stretch ratio λ of the original length. During this loading stage, boundary displacements are prescribed to control the overall stretch ratio, and the reaction force on the stretched surfaces is computed at different stretch ratios.

The circles in Figure 4 represent the roller boundary condition, which allows the boundary surface to slide along the in-plane surface tangential directions (z or x) while the deformation is restrained in the out-of-plane direction. The loading method here is designed to mimic the loading procedures widely used in experiments [55], where a small block of muscle tissue material is dissected and tested.

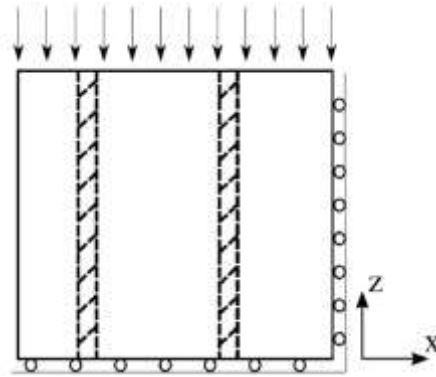


Figure 4 The 2D diagram (lateral view) of the muscle model under uniaxial loading, where the striated areas represent the connective tissues, the blank areas represent the muscle fibers, the circles represent the roller boundary condition, and the arrows pointing downward on the top surface indicates concentric contraction (pointing upward for eccentric contraction).

3. Results and Discussions

3.1. Numerical Validation

To validate the selected material parameters for the passive components of muscle tissue (fiber's passive part and CT) during ageing process, as listed in Table 1 - 4, a quasi-static numerical test is performed by applying uniaxial tensile loading to muscle tissue in the muscle fiber direction with different PS parameters (see Table 1 - 4). Figure 5 shows the comparison of stress-stretch relations between the numerical results and the experimental data measured from rat tibialis anterior muscles [56,57] and rabbit extensor digitorum longus muscles [58]. The grey shaded area in the figure depicts the standard deviation of the experimental data by Calvo et al. [57]. The experimental data shows a wide range of tensile response variations, and the numerical results of the proposed muscle tissue models with three sets of passive stiffness parameters listed in Table 4 lie within the range of the experimental stress-stretch response. The agreement between numerical and experimental results validates the proper selection of the material parameters for different passive components during ageing process, which will be used in the study of force generation mechanisms in Section 3.2.

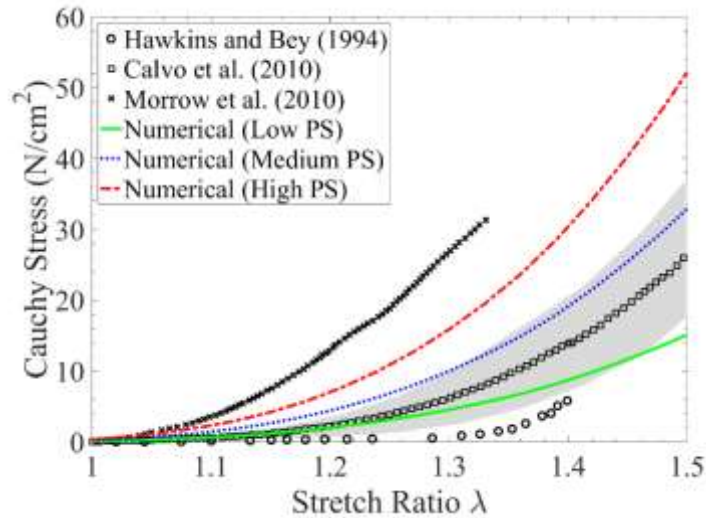


Figure 5 The comparison of experimental data and numerical results of muscle tissue under uniaxial tensile loading in the muscle fiber direction due to different muscle PS defined in Table 4, where the grey shaded area depicts the standard deviation of the experimental data [57]. “Thin CT” thickness is used for the numerical test (see Section 3.2.2 for more details).

3.2. Numerical Investigation of Force Generation

The pixel-based, cellular-scale micromechanical RKPM model described in Section 2.1 is used to study the causal relations between age-related microstructural variations in geometries and properties (including the passive stiffness of muscle, the thickness of CT, and the maximum isometric stress of muscle fibers) and macroscopic behaviors such as force generation capacity of skeletal muscles.

3.2.1. Effects of Passive Stiffness (PS)

The effect of PS on the force generation capacity of skeletal muscle under concentric and eccentric contraction is first investigated. Let us consider a muscle unit, as shown in Figure 7, where CT thickness of 18% volume ratio (refer to Section 3.2.2 for the study on CT thickness) and the fiber maximum isometric stress of 30 N/cm^2 are employed for simulations. The results of total force generation under concentric contraction by using different PS denoted in Table 4 is compared in Figure 6a. The results show that, at the same level of stretch, the muscle with higher PS generates

smaller force under concentric contraction ($\lambda < 1$). Note that when $\lambda = 1$ the muscle is undeformed and the passive components (fiber's passive part and CT) do not contribute to the muscle's force generation; thus, it yields the same force generation given we maintain active muscle properties constant in this example. On the other hand, when the muscle units are under eccentric contraction ($\lambda > 1$), as shown Figure 6b, the muscle with higher PS generates larger force, opposite to the case with concentric contraction. Mechanically, this opposite phenomenon can be explained by the superposition of reaction force from passive components and active force from fibers. Note that higher PS yields greater reaction stress (tensile or compressive) under external loading (eccentric and concentric). Therefore, under eccentric contraction, muscle units generate a larger total force as the stress exerted by tensile action in fibers is further increased by a larger tensile stress in the passive components with larger higher PS. On the contrary, under concentric contraction, the stress from fiber tensile action is “compensated” by the compressive stress in passive components, and thus the muscle unit with higher PS yields less force. These effects can be visualized from stress distributions at the final configuration of simulation during concentric contraction (see Figure 7). As can be seen, the fiber phase generates tensile stress (positive) and the CT phase shows compressive stress (negative) for all three cases, and thus the force from active tensile stress in fibers is offset by the force from passive compressive stress in the CTs. As a result, the muscle unit with stiffer CT (i.e., higher PS) generates less force, as illustrated in Figure 6a. The opposite trend in force generation under eccentric contraction (see Figure 6b) can be explained under a similar reasoning.

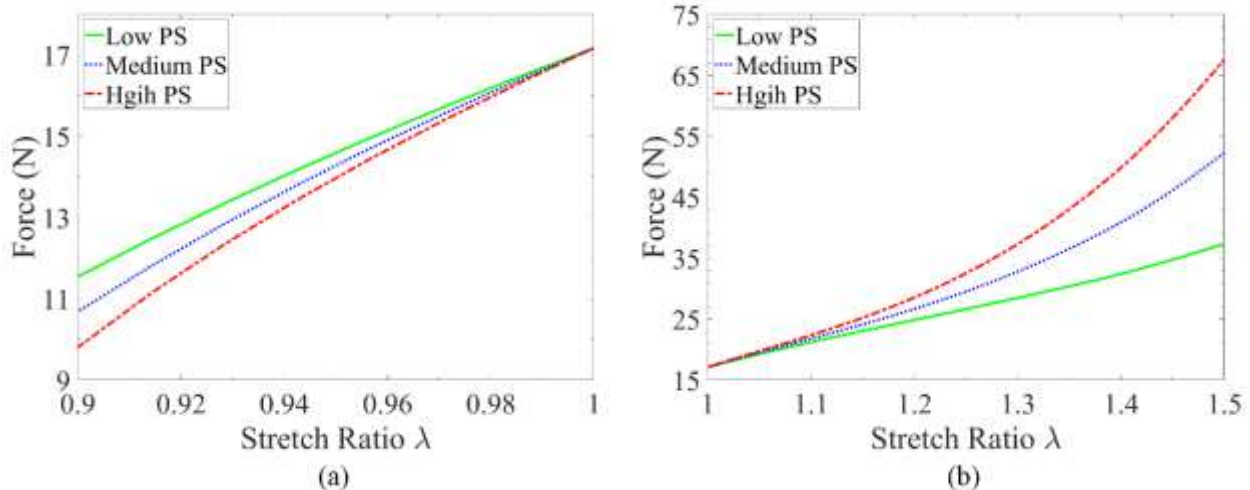


Figure 6 The comparison of force generation for muscle tissue with three different passive stiffness (PS) (a) when the muscle tissue shortens and (b) when the muscle tissue lengthens. The force is the total reaction force calculated on the loading boundary. The “Thin” CT is used for the CT phase and $\sigma_{\max} = 30 \text{ N/cm}^2$ is used for the fiber phase.

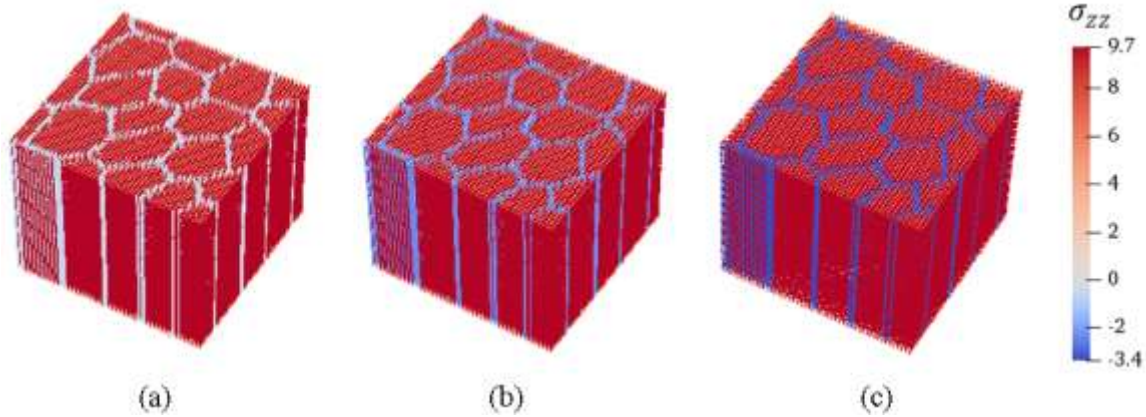


Figure 7 The distribution of the Cauchy stress component σ_{zz} (the muscle fiber direction) at the final configuration under concentric contraction. Figures (a), (b) and (c) are respectively the results of “Low PS”, “Medium PS” and “High PS”.

3.2.2. Effects of CT Thickness

It was observed that the CT thickness of old muscles is about two to threefold of that of young muscles [15,17]. To examine the effect of this microstructural change of CT thickness, muscles with three different CT thicknesses are considered in Figure 8. Lieber et al. reported that the fiber volume ratios are $38.5 \pm 13.6\%$ and $95.0 \pm 8.8\%$ for spastic muscle and healthy muscle, respectively [59]. Considering that ageing muscle preserves fibers better than spastic muscle, we take the range of CT volume ratios as 10 - 40%. As illustrated in Figure 8a-c, the CT volume ratios of “Thin CT”, “Medium Thick CT”, and “Thick CT” are 18%, 25%, and 36%, respectively. In the following simulations, the “High PS” and the fiber maximum isometric stress of 30 N/cm^2 are employed.

Figure 9 shows the influences of the CT thickness on the muscle's force generation capacity during concentric and eccentric contraction. The muscle unit with a larger volume ratio of CT always generates smaller force under concentric contraction. During eccentric contraction, however, the results show a more complex trend. There exists a critical stretch level (around $\lambda = 1.6$ in this case), and beyond that, the muscle tissue with thicker CT generate larger force. This is because the increase in the passive force due to thicker CT surpasses the decrease in the active force due to reduced volume ratio of muscle fibers beyond the critical stretch. Compared to the effects of passive stiffness, as shown in Figure 6, the influence of CT thickness on force generation is relatively less significant. Overall, the critical stretch is influenced by many factors, such as fiber contractile ability, muscle structural composition (volume ratio of components), and stiffness of muscle components.

The muscle fiber phase and the surrounding CT phase work together to generate force. As the muscle fibers and surrounding CT are strictly bonded at their interfaces [60,61], the CT deforms synchronously when the activated muscle fibers shorten. Subsequently, the CT, as the passive material, shortens with compressive force to resist shortening deformations. As muscle fiber contracts, stiffer CT resists with larger compressive force during concentric contraction, leading to reduced total force generated by the muscle tissue under concentric deformation. The trend is opposite for the eccentric contraction as both muscle fibers and CT exhibit tensile forces in this case and stiffer CT yields larger tensile force, leading to greater total force generation. Note that the stiffer CT can be due to larger hyperelastic constants or thicker CT thickness, and vice versa for the softer CT.

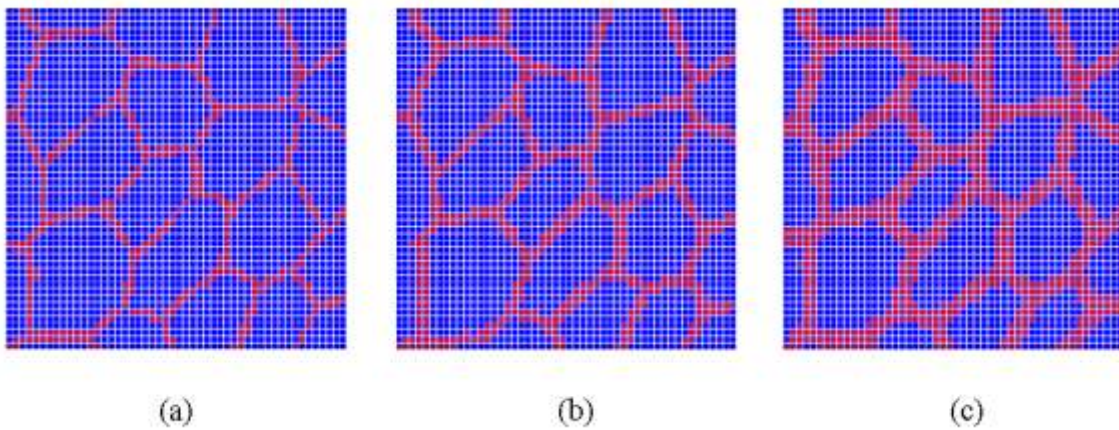


Figure 8 Honeycomb-like models of skeletal muscle tissue with different volume ratios of connective tissue (CT), which are respectively denoted by “Thin CT”, “Medium Thick CT”, and “Thick CT”. The corresponding CT volume ratios are 18%, 25%, and 36%, respectively. The red nodes represent CT material and the blue nodes represent muscle fiber material.

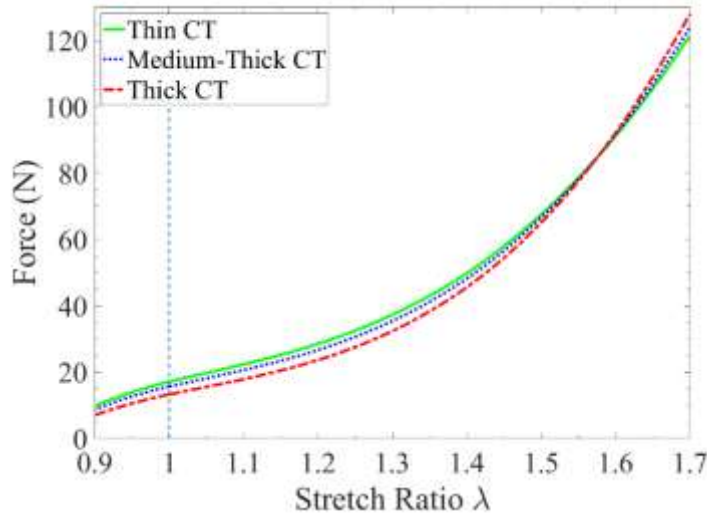


Figure 9 The comparison of force generation of muscle tissues with different connective tissue (CT) thickness. The muscle units with “High PS” and $\sigma_{\max} = 30 \text{ N/cm}^2$ are employed.

3.2.3. Effects of Fiber Maximum Isometric Stress

Apart from the microstructural changes in the passive components, the loss of muscle’s force generation capacity can result from other age-associated factors, such as the decreased force generation capacity of muscle fibers [62]. It was reported that the specific force generated by muscle fiber decreases by around 30% with ageing [63]. Furthermore, the range of values of the fiber maximum isometric stress commonly used in modeling skeletal muscle is from 22 N/cm² to 30 N/cm² [64]. In this study, the fiber maximum isometric stress with values of 30 N/cm², 26 N/cm², and 22 N/cm² is adopted in the muscle fiber model (Eq.(3)) to represent the Young, Adult, and Old cases, respectively. Here, the muscle passive stiffness and CT thickness employed in the simulations are the “Medium PS” and the “Medium Thick CT”, respectively. The numerical results

are shown in Figure 10, which show that the muscle tissues with higher fiber maximum isometric stress generate larger force during both concentric and eccentric contractions.

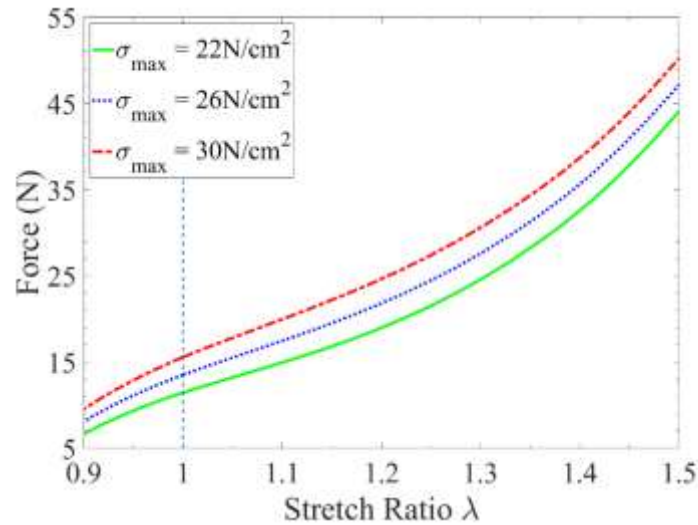


Figure 10 The comparison of force generation for muscle tissues with different fiber maximum isometric stresses. The “Medium PS” and “Medium Thick” CT are used.

3.2.4. Effects of Combined Factors

The numerical studies above have shown the individual effects of muscle passive stiffness, CT thickness, and fiber maximum isometric stress, on the muscle’s force generation capacity. Finally, the combined effects of all these age-related microstructural changes are examined. To simulate the ageing process, three age groups, i.e., “Young”, “Adult”, and “Old”, are designed and their material properties are summarized in Table 5. The results shown in Figure 11 agree with the trend observed in experiments, i.e. the skeletal muscle with ageing tends to maintain force generation capability during eccentric contraction, and the decrease in force production is more for concentric contraction than isometric contraction [9]. Figure 11 shows that with ageing the reduction of force generation (from Young to Old) is about 60% ($\lambda = 0.9$) under concentric contraction, whereas it is about 3% ($\lambda = 1.3$) to 35% ($\lambda = 1.1$) under eccentric contraction.

Table 5 - Material properties for modeling the ageing process, where the passive stiffness corresponds to Table 4 and the volume ratio of CT corresponds to Figure 8.

Age	Young	Adult	Old
σ_{\max} (N/cm ²)	30	26	22
Passive Stiffness	Low	Medium	High
Volume Ratio of CT	Thin	Medium Thick	Thick

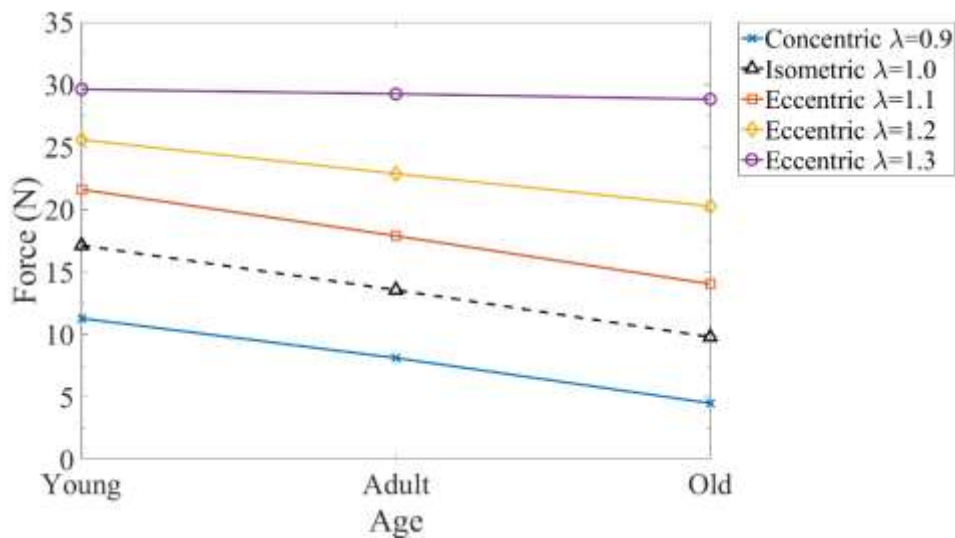


Figure 11 The ageing effects of the combined factors on force generation capacity of muscle tissues.

4. Conclusions

In this study, a honeycomb-like cellular-scale microstructural muscle model is developed to investigate the causal relations between age-related microstructural changes and the reduction in force generation capacity of skeletal muscle by using a pixel-based meshfree RKPM computational framework. By employing cellular-scale muscle units composed of muscle fibers and CT, the ‘intrinsic’ force generation capability can be examined and the mechanisms in force generation can be explained.

The numerical experiments performed here reveal that the muscle tissues with higher passive stiffness (stiffer CT phase) generate smaller force during concentric contraction, as the CT in the compressive state offsets the total force generation. On the contrary, during eccentric contraction, the muscle tissue with higher passive stiffness (stiffer CT and fiber's passive part) tends to enhance force generation due to a greater tensile force contributed from the passive components. The volume ratio of CT is also demonstrated to have similar effects on the force generation, but its enhancement effect on force generation occurs only when the stretch ratio is beyond a certain point, indicating a nonlinear influence from the variation of the microstructure geometry. Furthermore, it is shown that the reduction in the force capacity of muscle fiber (i.e. maximum isometric stress) reduces force generation under both concentric and eccentric contraction.

As the passive components, CT and fiber's passive part, have a strong contribution to the passive stiffness of skeletal muscle, their age-related material stiffening usually results in the increase of the overall passive stiffness of skeletal muscle, which is considered as one of the major factors accounting for the fact that skeletal muscle tends to maintain force generation capacity during eccentric contraction and reduce generation capacity during concentric contraction. Finally, the combined effects of age-related changes in all three factors (muscle passive stiffness, endomysium thickness, and specific muscle fiber force) on muscle's force generation capacity are demonstrated to agree with the experimental observation, i.e., the age-associated reduction in skeletal muscle force generation is greater under concentric contraction than eccentric contraction.

The cellular-scale microstructural muscle models used in this study are constructed from histological cross-sectional images enabling us to create realistic models of the in-vivo structure. The numerical results offer a deep insight into the mechanism on how the skeletal muscle tissues work and how the connective tissue and muscle fiber phases coordinate and contribute to the overall active force generation. The computational method used in this study also demonstrates the effectiveness of the meshfree RKPM image-based models, where no geometry reconstruction and mesh generation of complex microstructures is involved in the construction of the simulation model.

With the RKPM pixel-based method, the proposed honeycomb-like microstructural muscle models can be easily extended to investigate the effects of age- or disease-associated alterations in

microstructure on muscle's macroscopic functional properties. It should be noted that the force generation of skeletal muscle is influenced by some other factors that have not been considered in this study. These include alterations in regional fiber properties and distribution, changes in velocity and history dependent contractile properties of muscle fiber, loss of motor units, etc., and they demand a more comprehensive investigation in their influence on muscle force generation [1,65]. For instance, Seydewitz et al. proposed a multi-scale constitutive model considering velocity and history effects by a dynamic function at the microscale model of fiber activation [66]. Moreover, the giant protein, titin, plays an important role in both passive and active force production and transmission of muscle, and its activation-dependent behavior links closely to the history dependent behavior of muscle (residual force enhancement) [43,49]. Previous studies have demonstrated that titin stiffness increases during muscle activation with varying titin isoforms during muscle development [43,47], which is expected to be co-responsible for the differences in muscle's force generation between concentric and eccentric contractions. In the future, more sophisticated multi-scale constitutive models for both active and passive components of muscle will be introduced, e.g., a sub-cellular scale model to account for the effects of titin and an anisotropic model to consider the effects of collagen fibers of ECM. Apart from active and passive muscle properties, three-dimensional muscle architecture also plays an important role in muscular contraction dynamics. Muscle morphology (e.g., muscle dimension, pennation angle, muscle fascicle architecture, aponeurosis dimension, tendon-muscle fascicle length ratios, etc.) changes during ageing and thus influences muscular functionalities (e.g., force production and transmission) [67–69]. However, to what extent the above-listed muscle structural changes during ageing are related to mechanical properties and functionalities of muscle has not been understood thoroughly [69,70]. This requires more comprehensive investigation using 3D skeletal muscle models incorporated with the age-associated changes in muscle morphology.

Conflict of Interest Statement

None

Acknowledgment

The support of this work by the National Institute of Health under grant number

1 R01 AG056999-01A1 to the University of California, San Diego is very much appreciated.

Appendix A

In the meshfree reproducing kernel particle method (RKPM) [30,31] simulation, the skeletal muscle structure is discretized by a set of nodes, which is different from the mesh-based discretization used in the finite element method. This unique point-based discretization provides a natural way of constructing models using pixel points in MRI or CT scan images and avoids complexities involved in geometry reconstruction and mesh generation. Therefore, RKPM is preferred for the image-based numerical simulation.

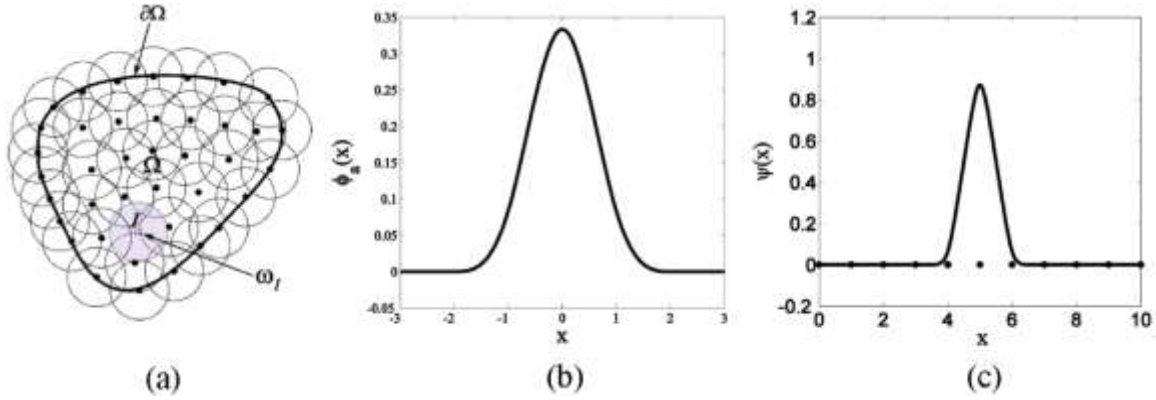


Figure 12 (a) Meshfree discretization of an object over the domain Ω ; (b) A cubic B-spline function widely used as kernel function; (c) An example of RK approximation function centered at $x = 5.0$ and with support size $a = 1.5 \times$ (nodal spacing).

The reproducing kernel (RK) approximation functions are formulated to possess desired completeness and continuity, which are respectively determined by using proper basis function and kernel function so that certain degree of accuracy and continuity in the approximation are achieved. As shown in Figure 12a, let a domain Ω be discretized by a set of ‘ NP ’ nodes and each node \mathbf{x}_I be associated with an approximation function $\Psi_I(\mathbf{x})$. For simulation, the displacement field is given by the RK approximation, denoted as u^h , is given by

$$u^h(\mathbf{x}) = \sum_{I=1}^{NP} \Psi_I(\mathbf{x})d_I, \quad (7)$$

where d_I is the nodal coefficient associated with the I -th node. The RK approximation function Ψ_I is expressed as

$$\Psi_I(\mathbf{x}) = C(\mathbf{x}; \mathbf{x} - \mathbf{x}_I) \phi_a(\mathbf{x} - \mathbf{x}_I) \quad (8)$$

where $\phi_a(\mathbf{x} - \mathbf{x}_I)$ is a kernel function which defines a local support for the approximation function measured by support size ‘ a ’ as well as its smoothness. For example, the cubic B-spline function is widely used as kernel function in RKPM, see Figure 12b,

$$\phi_a(z) = \begin{cases} \frac{2}{3} - 4z^2 + 4z^3; & \text{for } 0 \leq z < \frac{1}{2} \\ \frac{4}{3} - 4z + 4z^2 - \frac{4}{3}z^3; & \text{for } \frac{1}{2} \leq z < 1 \\ 0; & \text{for } z \geq 1 \end{cases} \quad (9)$$

where $z = \|\mathbf{x} - \mathbf{x}_I\|/a$. The term $C(\mathbf{x}; \mathbf{x} - \mathbf{x}_I)$ is a correction function constructed using a set of basis functions,

$$C(\mathbf{x}; \mathbf{x} - \mathbf{x}_I) = \sum_{i+j+k=0}^n (x_1 - x_{1I})^i (x_2 - x_{2I})^j (x_3 - x_{3I})^k b_{ijk}(\mathbf{x}) = \mathbf{H}^T(\mathbf{x} - \mathbf{x}_I) \mathbf{b}(\mathbf{x}) \quad (10)$$

in which $\mathbf{H}(\mathbf{x} - \mathbf{x}_I)$ is a vector containing all the monomial basis functions, n is the order of the complete monomials, and $\mathbf{b}(\mathbf{x})$ is an unknown parameter vector determined by enforcing the n -th order reproducing conditions as below,

$$\sum_{l=1}^{NP} \Psi_l(\mathbf{x}) x_{1l}^i x_{2l}^j x_{3l}^k = x_1^i x_2^j x_3^k; \quad |i + j + k| = 0, 1, \dots, n \quad (11)$$

In this work, a linear basis is used such that $\mathbf{H}^T(\mathbf{x} - \mathbf{x}_I) = [1, (x_1 - x_{1I}), (x_2 - x_{2I}), (x_3 - x_{3I})]$. Introducing Eqs. (9) and (10) into Eq. (11), the unknown vector can be obtained by $\mathbf{b}(\mathbf{x}) = \mathbf{M}^{-1}(\mathbf{x}) \mathbf{H}(\mathbf{0})$, where $\mathbf{M}(\mathbf{x})$ is the moment matrix given by,

$$\mathbf{M}(\mathbf{x}) = \sum_{l=1}^{NP} \mathbf{H}(\mathbf{x} - \mathbf{x}_l) \mathbf{H}^T(\mathbf{x} - \mathbf{x}_l) \phi_a(\mathbf{x} - \mathbf{x}_l). \quad (12)$$

Finally, the RK approximation function (see Figure 12c) is expressed as,

$$\Psi_I(\mathbf{x}) = \mathbf{H}^T(\mathbf{0}) \mathbf{M}^{-1}(\mathbf{x}) \mathbf{H}(\mathbf{x} - \mathbf{x}_I) \phi_a(\mathbf{x} - \mathbf{x}_I) \quad (13)$$

Note that the above RK approximation function does not possess the Kronecker delta property. Therefore, certain techniques are needed for RK approximation to have the kinematically admissible property and properly impose essential boundary conditions, such as transformation [31,71,72], coupling with finite elements near essential boundary [73,74], penalty method [75], Nitsche’s method [76–78], the modified variational principle [79], or the Lagrange multiplier method [80].

Reference

1. Ballak SB, Degens H, de Haan A, Jaspers RT. Aging related changes in determinants of muscle force generating capacity: A comparison of muscle aging in men and male rodents. *Ageing Research Reviews* 2014; **14**:43–55. doi:10.1016/j.arr.2014.01.005.
2. Power GA, Dalton BH, Rice CL. Human neuromuscular structure and function in old age: A brief review. *Journal of Sport and Health Science* 2013; **2**(4):215–226. doi:10.1016/j.jshs.2013.07.001.
3. Rahemi H, Nigam N, Wakeling JM. The effect of intramuscular fat on skeletal muscle mechanics: Implications for the elderly and obese. *Journal of the Royal Society Interface* 2015; **12**(109):20150365. doi:10.1098/rsif.2015.0365.
4. Porter MM, Myint A, Kramer JF, Vandervoort AA. Concentric and eccentric knee extension strength in older and younger men and women. *Canadian Journal of Applied Physiology* 1995; **20**(4):429–439. doi:10.1139/h95-034.
5. Power GA, Rice CL, Vandervoort AA. Increased Residual Force Enhancement in Older Adults Is Associated with a Maintenance of Eccentric Strength. *Public Library of Science One* 2012; **7**(10):e48044. doi:10.1371/journal.pone.0048044.
6. Brooks S V, Faulkner JA. Isometric, shortening, and lengthening contractions of muscle fiber segments from adult and old mice. *American Journal of Physiology* 1994; **267**(2):C507–C513. doi:10.1016/j.jep.2004.09.043.
7. Barber LA, Barrett RS, Gillett JG, Cresswell AG, Lichtwark GA. Neuromechanical properties of the triceps surae in young and older adults. *Experimental Gerontology* 2013; **48**(11):1147–1155. doi:10.1016/j.exger.2013.07.007.
8. Porter MM, Vandervoort AA, Kramer JF. Eccentric peak torque of the plantar and dorsiflexors is maintained in older women. *Journals of Gerontology - Series A Biological Sciences and Medical Sciences* 1997; **52**(2):B125–B131. doi:10.1093/gerona/52A.2.B125.
9. Roig M, MacIntyre DL, Eng JJ, Narici M V., Maganaris CN, Reid WD. Preservation of eccentric strength in older adults: Evidence, mechanisms and implications for training and rehabilitation. *Experimental Gerontology* 2010; **45**(6):400–409.
10. Purslow PP. The structure and functional significance of variations in the connective tissue within muscle. *Comparative Biochemistry and Physiology - A Molecular and Integrative Physiology* 2002; **133**(4):947–966. doi:10.1016/S1095-6433(02)00141-1.
11. Gillies AR, Lieber RL. Structure and function of the skeletal muscle extracellular matrix. *Muscle and Nerve* 2011; **44**(3):318–331. doi:10.1002/mus.22094.
12. Lieber RL, Steinman S, Barash IA, Chambers H. Structural and functional changes in spastic skeletal muscle. *Muscle and Nerve* 2004; **29**(5):615–627. doi:10.1002/mus.20059.
13. Purslow PP, Trotter JA. The morphology and mechanical properties of endomysium in series-fibred muscles: variations with muscle length. *Journal of Muscle Research and Cell*

- Motility* 1994; **15**(3):299–308. doi:10.1007/BF00123482.
14. Huijing PA. Muscle as a collagen fiber reinforced composite: A review of force transmission in muscle and whole limb. *Journal of Biomechanics* 1999; **32**(4):329–345. doi:10.1016/S0021-9290(98)00186-9.
 15. Alnaqeeb MA, Al Zaid NS, Goldspink G. Connective tissue changes and physical properties of developing and ageing skeletal muscle. *Journal of Anatomy* 1984; **139**(Pt 4):677. doi:10.1016/j.arr.2014.01.005.
 16. Gao Y, Kostrominova TY, Faulkner JA, Wineman AS. Age-related changes in the mechanical properties of the epimysium in skeletal muscles of rats. *Journal of Biomechanics* 2008; **41**(2):465–469. doi:10.1016/j.jbiomech.2007.09.021.
 17. Zhang C, Gao Y. Effects of aging on the lateral transmission of force in rat skeletal muscle. *Journal of Biomechanics* 2014; **47**(5):944–948. doi:10.1016/j.jbiomech.2014.01.026.
 18. Wood LK, Kayupov E, Gumucio JP, Mendias CL, Claflin DR, Brooks S V. Intrinsic stiffness of extracellular matrix increases with age in skeletal muscles of mice. *Journal of Applied Physiology* 2014; **117**(4):363–369. doi:10.1152/jappphysiol.00256.2014.
 19. Zajac FR. Muscle and tendon: properties, models, scaling, and application to biomechanics and motor control. *Critical Reviews in Biomedical Engineering* 1989; **17**(4):359–411. doi:10.1016/j.pcad.2015.11.006.
 20. Blemker SS, Delp SL. Three-Dimensional Representation of Complex Muscle Architectures and Geometries. *Annals of biomedical engineering* 2005; **33**(5):661–673. doi:10.1007/s10439-005-1433-7.
 21. Chi SW, Hodgson J, Chen JS, et al. Finite element modeling reveals complex strain mechanics in the aponeuroses of contracting skeletal muscle. *Journal of Biomechanics* 2010; **43**(7):1243–1250. doi:10.1016/j.jbiomech.2010.01.005.
 22. Johansson T, Meier P, Blickhan R. A finite-element model for the mechanical analysis of skeletal muscles. *Journal of Theoretical Biology* 2000; **206**(1):131–149. doi:10.1006/jtbi.2000.2109.
 23. Lemos RR, Epstein M, Herzog W, Wyvill B. A framework for structured modeling of skeletal muscle. *Computer Methods in Biomechanics and Biomedical Engineering* 2004; **7**(6):305–317. doi:10.1080/10255840412331317398.
 24. Böl M, Reese S. Micromechanical modelling of skeletal muscles based on the finite element method. *Computer Methods in Biomechanics and Biomedical Engineering* 2008; **11**(5):489–504. doi:10.1080/10255840701771750.
 25. Martins JAC, Pires EB, Salvado R, Dinis PB. A numerical model of passive and active behavior of skeletal muscles. *Computer Methods in Applied Mechanics and Engineering* 1998; **151**(3–4):419–433. doi:10.1016/S0045-7825(97)00162-X.

26. Sharafi B, Blemker SS. A micromechanical model of skeletal muscle to explore the effects of fiber and fascicle geometry. *Journal of Biomechanics* 2010; **43**(16):3207–3213. doi:10.1016/j.jbiomech.2010.07.020.
27. Virgilio KM, Martin KS, Peirce SM, Blemker SS. Multiscale models of skeletal muscle reveal the complex effects of muscular dystrophy on tissue mechanics and damage susceptibility. *Interface Focus* 2015; **5**(2):20140080. doi:10.1098/rsfs.2014.0080.
28. Spyrou LA, Agoras M, Danas K. A homogenization model of the Voigt type for skeletal muscle. *Journal of Theoretical Biology* 2017; **414**:50–61. doi:10.1016/j.jtbi.2016.11.018.
29. Spyrou LA, Brisard S, Danas K. Multiscale modeling of skeletal muscle tissues based on analytical and numerical homogenization. *Journal of the mechanical behavior of biomedical materials* 2019; **92**:97–117.
30. Liu WK, Jun S, Zhang YF. Reproducing kernel particle methods. *International Journal for Numerical Methods in Fluids* 1995; **20**(8–9):1081–1106. doi:10.1002/flid.1650200824.
31. Chen JS, Pan C, Wu CT, Liu WK. Reproducing Kernel Particle Methods for large deformation analysis of non-linear structures. *Computer Methods in Applied Mechanics and Engineering* 1996; **139**(1–4):195–227. doi:10.1016/S0045-7825(96)01083-3.
32. Chen JS, Yoon S, Wu CT. Non-linear version of stabilized conforming nodal integration for Galerkin mesh-free methods. *International Journal for Numerical Methods in Engineering* 2002; **53**(12):2587–2615. doi:10.1002/nme.338.
33. Basava RR, Chen JS, Zhang Y, et al. Pixel based meshfree modeling of skeletal muscles. In: *Lecture Notes in Computer Science (including subseries Lecture Notes in Artificial Intelligence and Lecture Notes in Bioinformatics)*; 2014:316–327.
34. Chen JS, Basava RR, Zhang Y, et al. Pixel-based meshfree modelling of skeletal muscles. *Computer Methods in Biomechanics and Biomedical Engineering: Imaging and Visualization* 2016; **4**(2):73–85. doi:10.1080/21681163.2015.1049712.
35. Chan TF, Vese LA. Active contours without edges. *IEEE Transactions on Image Processing* 2001; **10**(2):266–277. doi:10.1109/83.902291.
36. Fung Y. *Biomechanics: mechanical properties of living tissues*. Springer Science & Business Media; 2013.
37. Hughes TJR. Generalization of selective integration procedures to anisotropic and nonlinear media. *International Journal for Numerical Methods in Engineering* 1980; **15**(9):1413–1418. doi:10.1002/nme.1620150914.
38. Chen JS, Pan C, Wu CT. Large deformation analysis of rubber based on a reproducing kernel particle method. *Computational Mechanics* 1997; **19**(3):211–227. doi:10.1007/s004660050170.
39. Chen JS, Wu CT, Yoon S, You Y. A stabilized conforming nodal integration for Galerkin mesh-free methods. *International Journal for Numerical Methods in Engineering* 2001;

- 50(2):435–466. doi:10.1002/1097-0207(20010120)50:2<435::AID-NME32>3.0.CO;2-A.
40. Blemker SS, Pinsky PM, Delp SL. A 3D model of muscle reveals the causes of nonuniform strains in the biceps brachii. *Journal of Biomechanics* 2005; **38**(4):657–665. doi:10.1016/j.jbiomech.2004.04.009.
 41. Burkholder TJ, Lieber RL. Sarcomere length operating range of vertebrate muscles during movement. *The Journal of experimental biology* 2001. doi:10.1002/(sici)1097-4687(199610)230:1<69::aid-jmor6>3.0.co.
 42. Prado LG, Makarenko I, Andresen C, Krüger M, Opitz CA, Linke WA. Isoform diversity of giant proteins in relation to passive and active contractile properties of rabbit skeletal muscles. *Journal of General Physiology* 2005; **126**(5):461–480. doi:10.1085/jgp.200509364.
 43. Herzog W. The multiple roles of titin in muscle contraction and force production. *Biophysical Reviews* 2018; **10**(4):1187–1199.
 44. Bleiler C, Castañeda PP, Röhrle O. A microstructurally-based, multi-scale, continuum-mechanical model for the passive behaviour of skeletal muscle tissue. *Journal of the mechanical behavior of biomedical materials* 2019; **97**:171–186.
 45. Rahemi H, Nigam N, Wakeling JM. Regionalizing muscle activity causes changes to the magnitude and direction of the force from whole muscles—a modeling study. *Frontiers in Physiology* 2014; **5**:298. doi:10.3389/fphys.2014.00298.
 46. Yeoh OH. Some Forms of the Strain Energy Function for Rubber. *Rubber Chemistry and Technology* 1993; **66**(5):754–771. doi:10.5254/1.3538343.
 47. Ottenhejm CAC, Knottnerus AM, Buck D, et al. Tuning passive mechanics through differential splicing of titin during skeletal muscle development. *Biophysical journal* 2009; **97**(8):2277–2286.
 48. Heidlauf T, Röhrle O. Modeling the chemoelectromechanical behavior of skeletal muscle using the parallel open-source software library openCMISS. *Computational and Mathematical Methods in Medicine* 2013; **2013**. doi:10.1155/2013/517287.
 49. Heidlauf T, Klotz T, Rode C, Siebert T, Röhrle O. A continuum-mechanical skeletal muscle model including actin-titin interaction predicts stable contractions on the descending limb of the force-length relation. *PLoS Computational Biology* 2017; **13**(10). doi:10.1371/journal.pcbi.1005773.
 50. Bosboom EMH, Thomassen JAM, Oomens CWJ, et al. A numerical-experimental approach to determine the transverse mechanical properties of skeletal muscle. 2001:187–192.
 51. Bosboom EMH, Hesselink MKC, Oomens CWJ, Bouten CVC, Drost MR, Baaijens FPT. Passive transverse mechanical properties of skeletal muscle under in vivo compression. *Journal of biomechanics* 2001; **34**(10):1365–1368.

52. Grieve AP, Armstrong CG. Compressive properties of soft tissues. *Biomechanics XI-A. International Series on Biomechanics. Free University Press, Amsterdam* 1988:531–536.
53. Van Loocke M, Lyons CG, Simms CK. A validated model of passive muscle in compression. *Journal of biomechanics* 2006; **39**(16):2999–3009.
54. Zheng Y-P, Mak AFT, Lue B. Objective assessment of limb tissue elasticity: development of a manual indentation procedure. *Journal of rehabilitation research and development* 1999.
55. Böl M, Ehret AE, Leichsenring K, Weichert C, Kruse R. On the anisotropy of skeletal muscle tissue under compression. *Acta Biomaterialia* 2014; **10**(7):3225–3234. doi:10.1016/j.actbio.2014.03.003.
56. Hawkins D, Bey M. A comprehensive approach for studying muscle-tendon mechanics. *Journal of biomechanical engineering* 1994; **116**(1):51–55.
57. Calvo B, Ramirez A, Alonso A, et al. Passive nonlinear elastic behaviour of skeletal muscle: experimental results and model formulation. *Journal of biomechanics* 2010; **43**(2):318–325.
58. Morrow DA, Haut Donahue TL, Odegard GM, Kaufman KR. Transversely isotropic tensile material properties of skeletal muscle tissue. *Journal of the Mechanical Behavior of Biomedical Materials* 2010; **3**(1):124–129. doi:10.1016/j.jmbbm.2009.03.004.
59. Lieber RL, Runesson E, Einarsson F, Fridén J. Inferior mechanical properties of spastic muscle bundles due to hypertrophic but compromised extracellular matrix material. *Muscle and Nerve* 2003; **28**(4):464–471. doi:10.1002/mus.10446.
60. Street SF. Lateral transmission of tension in frog myofibers: A myofibrillar network and transverse cytoskeletal connections are possible transmitters. *Journal of Cellular Physiology* 1983; **114**(3):346–364. doi:10.1002/jcp.1041140314.
61. Street SF, Ramsey RW. Sarcolemma: Transmitter of active tension in frog skeletal muscle. *Science* 1965; **149**(3690):1379–1380. doi:10.1126/science.149.3690.1379.
62. Miljkovic N, Lim JY, Miljkovic I, Frontera WR. Aging of skeletal muscle fibers. *Annals of Rehabilitation Medicine* 2015; **39**(2):155. doi:10.5535/arm.2015.39.2.155.
63. Ochala J, Frontera WR, Dorer DJ, Van Hoecke J, Krivickas LS. Single skeletal muscle fiber elastic and contractile characteristics in young and older men. *Journals of Gerontology - Series A Biological Sciences and Medical Sciences* 2007; **62**(4):375–381. doi:10.1093/gerona/62.4.375.
64. Dao TT, Tho M-CHB. A Systematic Review of Continuum Modeling of Skeletal Muscles: Current Trends, Limitations, and Recommendations. *Applied bionics and biomechanics* 2018; **2018**.
65. Vandervoort AA. Aging of the human neuromuscular system. *Muscle and Nerve* 2002; **25**(1):17–25. doi:10.1002/mus.1215.

66. Seydewitz R, Siebert T, Böl M. On a three-dimensional constitutive model for history effects in skeletal muscles. *Biomechanics and Modeling in Mechanobiology* 2019;1–17. doi:10.1007/s10237-019-01167-9.
67. Kubo K, Kanehisa H, Azuma K, et al. Muscle architectural characteristics in women aged 20-79 years. *Medicine and Science in Sports and Exercise* 2003; **35**(1):39–44. doi:10.1097/00005768-200301000-00007.
68. Mörl F, Siebert T, Häufle D. Contraction dynamics and function of the muscle-tendon complex depend on the muscle fibre-tendon length ratio: a simulation study. *Biomechanics and Modeling in Mechanobiology* 2016; **15**(1):245–258. doi:10.1007/s10237-015-0688-7.
69. Siebert T, Tomalka A, Stutzig N, Leichsenring K, Böl M. Changes in three-dimensional muscle structure of rabbit gastrocnemius, flexor digitorum longus, and tibialis anterior during growth. *Journal of the Mechanical Behavior of Biomedical Materials* 2017; **74**:507–519. doi:10.1016/j.jmbbm.2017.07.045.
70. Bénard MR, Harlaar J, Becher JG, Huijing PA, Jaspers RT. Effects of growth on geometry of gastrocnemius muscle in children: A three-dimensional ultrasound analysis. *Journal of Anatomy* 2011; **219**(3):388–402. doi:10.1111/j.1469-7580.2011.01402.x.
71. Wagner GJ, Liu WK. Application of essential boundary conditions in mesh-free methods: A corrected collocation method. *International Journal for Numerical Methods in Engineering* 2000; **47**(8):1367–1379. doi:10.1002/(SICI)1097-0207(20000320)47:8<1367::AID-NME822>3.0.CO;2-Y.
72. Chen JS, Wang HP. New boundary condition treatments in meshfree computation of contact problems. *Computer Methods in Applied Mechanics and Engineering* 2000; **187**(3–4):441–468. doi:10.1016/S0045-7825(99)00335-7.
73. Krongauz Y, Belytschko T. Enforcement of essential boundary conditions in meshless approximations using finite elements. *Computer Methods in Applied Mechanics and Engineering* 1996; **131**(1–2):133–145. doi:10.1016/0045-7825(95)00954-X.
74. Fernández-Méndez S, Huerta A. Imposing essential boundary conditions in mesh-free methods. *Computer Methods in Applied Mechanics and Engineering* 2004; **193**(12–14):1257–1275. doi:10.1016/j.cma.2003.12.019.
75. Zhu T, Atluri SN. A modified collocation method and a penalty formulation for enforcing the essential boundary conditions in the element free Galerkin method. *Computational Mechanics* 1998; **21**(3):211–222. doi:10.1007/s004660050296.
76. Nitsche J. Über ein Variationsprinzip zur Lösung von Dirichlet-Problemen bei Verwendung von Teilräumen, die keinen Randbedingungen unterworfen sind. *Abhandlungen aus dem Mathematischen Seminar der Universität Hamburg* 1971; **36**(1):9–15. doi:10.1007/BF02995904.
77. Griebel M, Schweitzer MA. A Particle-Partition of Unity Method Part V: Boundary

- Conditions. In: *Geometric Analysis and Nonlinear Partial Differential Equations*; 2003:519–542.
78. Babuška I, Banerjee U, Osborn JE. Meshless and Generalized Finite Element Methods: A Survey of Some Major Results. In: *Meshfree methods for partial differential equations*; 2003:1–20.
79. Lu YY, Belytschko T, Gu L. A new implementation of the element free Galerkin method. *Computer Methods in Applied Mechanics and Engineering* 1994; **113**(3–4):397–414. doi:10.1016/0045-7825(94)90056-6.
80. Belytschko T, Lu YY, Gu L. Element-free Galerkin methods. *International Journal for Numerical Methods in Engineering* 1994; **37**(2):229–256. doi:10.1002/nme.1620370205.